

# Modeling Tropical Atmospheric Convection in the Context of the Weak Temperature Gradient Approximation

David J. Raymond\*

Physics Department and Geophysical Research Center,

New Mexico Tech, Socorro, NM, USA

Xiping Zeng,

Laboratory for Atmospheres, NASA/GSFC,

Greenbelt, MD, USA

October 30, 2005

## **Abstract**

A cumulus ensemble model is used to simulate the interaction between tropical atmospheric convection and the large-scale tropical environment in the context of Sobel and Bretherton's (2000) weak temperature gradient approximation. In this approximation gravity waves are assumed to redistribute buoyancy anomalies over a broad area of the tropics, thus maintaining the local virtual temperature profile close to the large-scale mean. This result is implemented in the model by imposing the advective effects of a hypothetical mean vertical velocity which is just sufficient to counteract the

---

\*Corresponding author email: [raymond@kestrel.nmt.edu](mailto:raymond@kestrel.nmt.edu)

local heating induced by convection and radiation. The implied vertical advection in the moisture equation and entrainment of air from the surrounding environment have major effects on the evolution of convection in the model.

The precipitation produced by the model mimics the results of a very simple model of tropical precipitation introduced by Raymond (2000), in that the mean rainfall rate predicted by the cumulus ensemble model is to a good approximation a function only of the mean column precipitable water. The evolution of the precipitable water, and hence the precipitation rate, is a result of the imbalance between the surface flux of moist entropy into the domain and the radiative loss of entropy out of the top of the domain. This evolution leads to a statistically steady solution in which the resulting precipitation rate is a unique function of the entropy flux imbalance. These results support the hypothesis that tropical precipitation averaged over distance scales of a few hundred kilometers and time scales of a day is a consequence only of local thermodynamic factors.

## 1 Introduction

Cumulus ensemble models have been useful in developing an understanding of deep, moist convection in the tropical atmosphere. The simplest way to use such models is in the radiative-convective equilibrium mode, in which convection is allowed to evolve in an environment cooled by the loss of thermal radiation and heated by surface heat fluxes. Examples of such calculations are those of Robe and Emanuel (1996; 2001), Tompkins and Craig (1998a,b; 1999), Tompkins (2001a,b), Grabowski and Moncrieff (2001), etc.

A characteristic of the radiative-convective equilibrium approach is that no connection with large-scale tropical dynamics is made. A commonly used one-way coupling is to impose vertical advective tendencies which mimic the effects of large-scale ascent or descent. The vertical motion is obtained from observations or from idealized assumptions. The response of the convection to these advective tendencies is then evaluated. Details of this method,

which is in widespread use (e. g., Sui et al., 1994; Grabowski et al., 1996, 1999; Grabowski et al., 1998; Xu and Randall, 1999; etc.), are presented by Randall et al. (1996).

In the deep tropics the large-scale vertical velocity is composed of the vertical mass flux in the convection plus a relatively constant clear air descent which follows from radiative cooling. Thus, vertical motion is largely a result of deep convection, and imposing the effects of an externally specified vertical velocity on a cumulus ensemble model introduces a chain of causality unlikely to be present in tropical convective development, due to the weakness of quasigeostrophic or other deep lifting processes there. Models using this technique are useful, but must be interpreted in an “inverse fashion”: By imposing the result (large-scale vertical velocity) one may inquire about the causes (principally the temperature and humidity profiles) leading to this result.

An alternate framework for linking cumulus ensemble models with large-scale tropical dynamics is provided by the weak temperature gradient approximation (WTG) of Sobel and Bretherton (2000). WTG derives the domain-averaged vertical velocity from the domain-averaged heating. This is done by assuming that the advection due to the vertical velocity is just sufficient to counteract the convective and radiative heating in the domain, thus keeping the mean virtual temperature profile fixed. The resulting vertical velocity is called the *WTG vertical velocity*. It is equivalent to the diabatic vertical velocity of Mapes and Houze (1995). The convection itself is assumed to be a function only of local conditions such as the temperature, humidity, and wind profiles, plus surface heat, moisture, and momentum fluxes, since these are the only things that convective cells “see”.

The WTG approximation applies where rotational effects are weak, i. e., near the equator. In this environment gravity waves constantly redistribute buoyancy anomalies so as to drive the atmosphere toward uniform virtual temperatures on isobaric surfaces. WTG assumes that this process is highly efficient, resulting in the assumption that isobaric temperature gradients and time tendencies are small enough to be ignored.

Since the vertical velocity follows from the convection in the WTG approximation, the

chain of causality is representative of that which actually occurs in the tropics. A cumulus ensemble model is thus useful in the context of the WTG approximation for investigations seeking how convection is forced by the tropical environment.

The WTG approximation is closely related to two-column models in which the convective ensembles in the two columns are subjected to different conditions, but are forced to maintain nearly equal mean temperature or pressure profiles (Nilsson and Emanuel, 1999; Raymond and Zeng, 2000). In the WTG model the reference virtual temperature profile is externally specified rather than being computed internally as a result of interactions between the two columns. This is simpler in that it allows greater control over the reference state in which the deep convection is embedded. An additional advantage over the two-column approach is that the amount of computation is cut in half.

Raymond (2000; referred to hereafter as R2000) developed a highly simplified model of tropical rainfall using the WTG approximation. This model, which is based on the earlier results of Neelin and Held (1987), postulates that the rainfall rate in the tropics is inversely proportional to the vertically averaged saturation deficit. In other words, the closer the atmosphere is to saturation, the harder it rains.

R2000 assumes that the tropical atmosphere adjusts to an excess in the total surface heat flux over the net outgoing radiative heat loss by exporting heat laterally. This lateral export is effected by the lateral inflows and outflows associated with deep convection. However, the time required for the environment to equilibrate after the balance between surface fluxes, radiation, and lateral export is upset is found to vary greatly depending on the pre-existing state of the atmosphere. For a moist atmosphere which is already strongly precipitating, this time scale is measured in hours, while for a dry, weakly convecting atmosphere, it can be tens of days.

In this paper we test the results of R2000 using a “toy” or highly simplified cumulus ensemble model developed in the context of the WTG approximation using the following strategy:

1. We first run the model to radiative-convective equilibrium with fixed mean surface winds and a sea surface temperature (SST) comparable to that existing in the tropics. In this calculation the potential temperature profile is unconstrained and the WTG vertical velocity is assumed to be zero. The results are used to provide a reference set of thermodynamic profiles.
2. We use the above-determined reference thermodynamic profiles to start WTG calculations in which some parameter such as mean surface wind or SST is altered from its radiative-convective equilibrium value.
3. Finally, we examine the adjustment of the convection and the precipitation it produces to the altered forcing.

We begin in section 2 with the weak temperature gradient and associated approximations and continue in section 3 with a description of the cumulus ensemble model. In section 4 we describe details of the modeling strategy, while section 5 presents the results. Conclusions appear in section 6 and the appendix presents details of the model which don't appear in section 3.

## 2 Model implementation of WTG approximation

We begin by splitting the total wind field  $\mathbf{v}_T$  into two parts:

$$\mathbf{v}_T = \mathbf{v} + \mathbf{v}_D, \tag{1}$$

each of which satisfies mass continuity separately. The component  $\mathbf{v}$  is the part of the wind computed explicitly in the cumulus ensemble model. This field obeys cyclic boundary conditions on the lateral model boundaries, and thus exhibits zero vertical mass flux averaged horizontally over the model domain.

The component  $\mathbf{v}_D$ , with horizontal and vertical parts  $\mathbf{v}_{Dh}$  and  $w_D$ , accounts for the mean vertical motion in the model and the associated horizontal flow needed to satisfy the anelastic mass continuity equation

$$\nabla \cdot (\bar{\rho} \mathbf{v}_{Dh}) + \frac{\partial(\bar{\rho} w_D)}{\partial z} = 0 \quad (2)$$

where  $\bar{\rho}(z)$  is the horizontally averaged density. Generally,  $|\mathbf{v}_D| \ll |\mathbf{v}|$ , so an approximate treatment of  $\mathbf{v}_D$  is justified. We assume that  $w_D$  is uniform over the domain of the cumulus ensemble model, i. e., it is a function only of  $z$  and  $t$ . We further assume that the horizontal average of  $\mathbf{v}_{Dh}$  is zero at each level. Thus, to the extent that the environment is sheared, this shear is carried by  $\mathbf{v}$  rather than  $\mathbf{v}_D$ . The treatment of  $\mathbf{v}_D$  in the thermodynamic equations of the cumulus ensemble model forms the crux of the interaction between modeled convection and the large scale.

The potential temperature equation takes the form

$$\frac{\partial \rho \theta}{\partial t} + \nabla \cdot (\rho \mathbf{v} \theta + \mathbf{T}_\theta) = \rho S_\theta - \nabla \cdot (\bar{\rho} \mathbf{v}_D \theta) \quad (3)$$

where  $\mathbf{T}_\theta$  represents unresolved eddy and viscous transport,  $S_\theta$  is the diabatic potential temperature source, and where we have approximated the full density  $\rho$  by the horizontally averaged density wherever it occurs in conjunction with  $\mathbf{v}_D$ . Further approximating  $\theta$  by its horizontal average  $\bar{\theta}$  on the right side of (3), this becomes

$$\frac{\partial \rho \theta}{\partial t} + \nabla \cdot (\rho \mathbf{v} \theta + \mathbf{T}_\theta) = \rho S_\theta - \bar{\rho} w_D \frac{\partial \bar{\theta}}{\partial z} \equiv \rho(S_\theta - E_\theta) \quad (4)$$

with the aid of (2).

The WTG approximation requires that the horizontal average of  $\partial \rho \theta / \partial t$  be zero over the ensemble model domain. We enforce this by equating  $E_\theta$  to an expression which causes the

horizontally averaged potential temperature to relax to a reference profile  $\theta_0(z)$ :

$$E_\theta = \lambda_t \sin(\pi z/h) [\bar{\theta} - \theta_0(z)]. \quad (5)$$

The relaxation is forced to occur at a height-dependent rate of  $\lambda_t \sin(\pi z/h)$ . The parameter  $h = 15$  km is the assumed height of the tropopause, so the sine function suppresses the relaxation at the surface and the tropopause. Above the tropopause the relaxation is set to zero. The purpose of this  $z$  dependence is to represent the fact that the buoyancy adjustment process due to gravity waves produced by deep convection is likely to be strongest in the middle troposphere.

Solving  $E_\theta = w_D (\partial \bar{\theta} / \partial z)$  for  $w_D$  results in

$$w_D = \frac{E_\theta}{(\partial \bar{\theta} / \partial z)}. \quad (6)$$

We call  $w_D$  the *WTG vertical velocity*. In the planetary boundary layer  $w_D$  is interpolated linearly from its value at the top of the boundary layer to zero at the surface. This is needed because, as Sobel and Bretherton (2000) point out, the weak temperature gradient approximation breaks down in the boundary layer. In this work we take the top of the boundary layer to be 1000 m, so that it includes the shallow layer of clouds often found over the ocean. In addition,  $\partial \bar{\theta} / \partial z$  is not allowed to become less than  $1 \text{ K km}^{-1}$  in the above equation. Under certain circumstances model feedbacks in the upper troposphere can otherwise result in very weak static stabilities and unrealistically large values of  $w_D$ . This imposed lower bound on the static stability is arbitrary and therefore must be viewed with some caution.

The introduction of a relaxation scheme to enforce the WTG approximation means that WTG isn't precisely obeyed in the model. However, it is not precisely obeyed in nature, and the sense of the deviation from WTG in the model should roughly mimic what happens in nature, e. g., strong heating should result in a temporarily warmer environment, etc.

An equation analogous to (3) may be written for the mixing ratio of the total advected water (vapor plus advected condensate such as cloud droplets):

$$\frac{\partial \rho r_t}{\partial t} + \nabla \cdot (\rho \mathbf{v} r_t + \mathbf{T}_r) = \rho S_r - \nabla_h \cdot (\bar{\rho} \mathbf{v}_{Dh} r_t) - \frac{\partial}{\partial z} (\bar{\rho} w_D r_t), \quad (7)$$

where  $S_r$  is the source of  $r_t$  due to precipitation production and evaporation. The last two terms on the right side of (7) represent respectively the entrainment of total advected water from the environment surrounding the cumulus ensemble model domain and the vertical transport of water by the large-scale vertical motion.

We treat the entrainment term by assuming that it can be replaced by its horizontally averaged value:

$$\nabla_h \cdot (\bar{\rho} \mathbf{v}_{Dh} r_t) \approx \frac{1}{A} \int \nabla_h \cdot (\bar{\rho} \mathbf{v}_{Dh} r_t) dA = \frac{1}{A} \oint r_t \bar{\rho} \mathbf{v}_{Dh} \cdot \mathbf{n} dl \quad (8)$$

where  $A$  is the horizontal area of the ensemble model domain and  $\mathbf{n}$  is the horizontal outward unit normal on the lateral domain boundary. The line integral is around the periphery of the domain. We now make a somewhat restrictive assumption for the purposes of this paper, namely that the convection takes place in an unsheared environment, so that in at least an approximate sense a positive value of  $\mathbf{v}_{Dh} \cdot \mathbf{n}$  (as opposed to a positive value of the outward normal component of total wind) indicates flow out of the ensemble domain, while the opposite sign indicates inflow. Since we define  $\bar{\mathbf{v}}_{Dh} = 0$ , we can insist that a positive or negative value of  $\mathbf{v}_{Dh} \cdot \mathbf{n}$  at one point on the periphery indicate a positive or negative value everywhere on the periphery. We further require that the outward-flowing air have a total advected water mixing ratio equal to the horizontally averaged value of this parameter inside the domain, i. e.,  $\bar{r}_t$ . For inflowing air we instead set the mixing ratio equal that of a reference profile  $r_0(z)$ . Defining  $r_x$  as being equal to  $\bar{r}_t$  when  $\mathbf{v}_{Dh} \cdot \mathbf{n}$  is positive and  $r_0$  when

$\mathbf{v}_{Dh} \cdot \mathbf{n}$  is negative, we use mass continuity to rewrite (8) as

$$\nabla \cdot (\bar{\rho} \mathbf{v}_{Dh} r_t) \approx -r_x \frac{\partial \bar{\rho} w_D}{\partial z}. \quad (9)$$

The last term in (7) can be approximated by assuming that  $r_t \approx \bar{r}_t$ , so that

$$\frac{\partial}{\partial z} (\bar{\rho} w_D r_t) \approx \bar{r}_t \frac{\partial \bar{\rho} w_D}{\partial z} + \bar{\rho} w_D \frac{\partial \bar{r}_t}{\partial z}, \quad (10)$$

resulting in

$$\frac{\partial \rho r_t}{\partial t} + \nabla \cdot (\rho \mathbf{v} r_t + \mathbf{T}_r) = \rho S_r - (\bar{r}_t - r_x) \frac{\partial \bar{\rho} w_D}{\partial z} - \bar{\rho} w_D \frac{\partial \bar{r}_t}{\partial z} \equiv \rho(S_r - E_r). \quad (11)$$

Note that  $r_x$  equals  $r_0(z)$  when  $\partial(\bar{\rho} w_D)/\partial z > 0$  and is equal to  $\bar{r}_t$  otherwise. In the latter case the entrainment term on the right side of (11) vanishes.

The terms

$$E_\theta = \lambda_t \sin(\pi z/h) [\bar{\theta} - \theta_0(z)] = w_D \frac{\partial \bar{\theta}}{\partial z}$$

and

$$E_r = \frac{(\bar{r}_t - r_x)}{\bar{\rho}} \frac{\partial \bar{\rho} w_D}{\partial z} + w_D \frac{\partial \bar{r}_t}{\partial z}$$

represent the thermodynamic interaction of the cumulus ensemble model with its surrounding environment. In conjunction with (6), they represent a closed system for this interaction. In a statistically steady state situation, they also represent the thermodynamic source terms for the large-scale flow due to small-scale and diabatic effects.

Given the simplified definition of  $\theta_e$  (see appendix) and the assumption that  $\bar{r}_t$  doesn't differ much from the domain-averaged mixing ratio, an equivalent term representing the interaction with the large-scale environment in the equivalent potential temperature equation

can be defined in terms of  $E_\theta$  and  $E_r$ :

$$E_e = (\bar{\theta}_e/\bar{\theta})E_\theta + \alpha\bar{\theta}_e E_r. \quad (12)$$

The overbars represent horizontal averages as above. This result is needed as the thermodynamics of the cumulus ensemble model are cast in terms of the total advected water and the equivalent potential temperature.

### 3 Cumulus ensemble model

The cumulus ensemble model is fully compressible and is implemented on a non-rotating, horizontally periodic domain. The treatment of precipitation formation and evaporation is very simple, with no distinction being made between liquid and ice processes. The model may be run in either two or three-dimensional mode.

Model details are presented in the appendix, but the basic governing equations are presented here. The mass continuity equation is

$$\frac{\partial \rho}{\partial t} + \nabla \cdot (\rho \mathbf{v}) = -\nu[p_0(0) - p_R]/(RT_R) \quad (13)$$

where  $\rho$  is the air density,  $\mathbf{v}$  is the part of the air velocity computed directly by the model (see the previous section), and the term to the right of the equals sign is a mass source term designed to relax the domain-averaged surface pressure  $p_0(0)$  to  $p_R = 1000$  hPa. This term is needed because the model domain is closed at the top by a rigid lid and laterally by periodic boundary conditions, resulting otherwise in a change in the mean pressure if the mean temperature changes. The quantity  $R$  is the gas constant for air,  $T_R = 300$  K is a constant reference temperature, and  $\nu = 0.001$  s<sup>-1</sup> is the assumed rate constant for mass adjustment.

The momentum equation ignores the effects of  $\mathbf{v}_D$  and is therefore written

$$\frac{\partial \rho \mathbf{v}}{\partial t} + \nabla \cdot (\rho \mathbf{v} \mathbf{v} - K \mathbf{D} - K_h \nabla_h \rho \mathbf{v}) + \nabla p + g \rho \mathbf{k} = \rho (\mathbf{F}_s - \mathbf{E}_m) - \mu (\mathbf{v}_h - \mathbf{v}_{h0}) \quad (14)$$

where  $K$  is the eddy mixing coefficient computed using a Smagorinsky-like scheme (see appendix),  $K_h$  is an additional constant horizontal eddy mixing coefficient for the suppression of high-frequency numerical modes,  $p$  is the pressure,  $g$  is the acceleration of gravity,  $\mathbf{F}_s$  is the force due to surface stresses,  $\mathbf{v}_h$  is the horizontal velocity,  $\mathbf{v}_{h0}(z)$  is an assumed reference velocity profile, and  $\mu(z)$  is an externally specified damping rate profile turned on only in the stratosphere for the purpose of damping upward-propagating gravity waves. At the top of the domain  $\mu = 0.1 \text{ s}^{-1}$ . This tapers linearly to zero at the assumed level of the tropopause. The deformation rate tensor  $\mathbf{D}$  is given by

$$D_{ij} = \frac{1}{2} \left( \frac{\partial v_i}{\partial x_j} + \frac{\partial v_j}{\partial x_i} \right). \quad (15)$$

The quantity  $\mathbf{E}_m$  represents a relaxation term which forces the mean wind profile toward the reference profile:

$$\mathbf{E}_m = \lambda_d [\bar{\mathbf{v}}_h - \mathbf{v}_{h0}(z)], \quad (16)$$

where  $\bar{\mathbf{v}}_h$  is the horizontally averaged horizontal wind and  $\lambda_d$  is the relaxation constant.

For the thermodynamic equation we have

$$\frac{\partial \rho \theta_e}{\partial t} + \nabla \cdot (\rho \mathbf{v} \theta_e - K \nabla \theta_e - K_h \nabla_h \rho \theta_e) = \rho (S_{es} + S_{er} - E_e) \quad (17)$$

where  $\theta_e$  is equivalent potential temperature,  $S_{es}$  is the source of equivalent potential temperature from surface fluxes,  $S_{er}$  is the source from radiation, and  $E_e$  is the external sink of equivalent potential temperature due to the interaction with the large-scale flow (see section

2). The equation for total advected water mixing ratio  $r_t$  is

$$\frac{\partial \rho r_t}{\partial t} + \nabla \cdot (\rho \mathbf{v} r_t - K \nabla r_t - K_h \nabla_h \rho r_t) = \rho (S_{cr} + S_{rs} - E_r) \quad (18)$$

where  $S_{cr}$  is minus the conversion rate of cloud water to precipitation,  $S_{rs}$  is the source of total cloud water mixing ratio from surface evaporation, and  $E_r$  represents the interaction with the large-scale flow. Finally, the equation for precipitation mixing ratio is

$$\frac{\partial \rho r_r}{\partial t} + \nabla \cdot [\rho (\mathbf{v} - w_t \mathbf{k}) r_r - K \nabla r_r - K_h \nabla_h \rho r_r] = -\rho S_{cr} \quad (19)$$

where  $w_t = 5 \text{ m s}^{-1}$  is the assumed hydrometeor terminal velocity. Due to the fact that inside cloud  $w_t \gg w_D$ , the effects of  $\mathbf{v}_D$  are negligible in this equation, and are ignored. The pressure is obtained diagnostically from the density and the potential temperature  $\theta$ :

$$p = (\rho R \theta)^\gamma / p_R^{\gamma-1} \quad (20)$$

where  $\gamma$  is the ratio of specific heats for air. The potential temperature is obtained iteratively from the equivalent potential temperature and the total cloud water mixing ratio.

Though the model is formulated in terms of equivalent potential temperature, we prefer to present results in terms of the moist entropy, in order to facilitate comparison with the observations of Raymond et al. (2003, hereafter R2003). We therefore define the dry, moist, and saturated moist entropy as follows:

$$s_d = C_p \ln(\theta/T_F) \quad (21)$$

$$s = C_p \ln(\theta_e/T_F) \quad (22)$$

$$s_s = C_p \ln(\theta_{es}/T_F) \quad (23)$$

where  $C_p$  is the specific heat of air at constant pressure, and where we set  $T_F = 273.15 \text{ K}$ ,

so as to maintain rough compatibility with the moist entropy defined by R2003.

## 4 Tropical oceanic simulations

In this section we develop the strategy outlined in the introduction for furthering our understanding of deep convection over tropical oceans. Though we are well aware of the potential problems of two-dimensional calculations of cumulus convection, we consider this work to be exploratory, and to conserve computer time we perform all calculations on a two-dimensional domain with horizontal and vertical dimensions of 50 km and 20 km respectively. This small domain is of ample size for individual convective cells. However, mesoscale convective organization does not have room to develop. The effects of expansion to larger domains and to three-dimensions will be explored in later work.

The vertical grid size is taken to be  $\Delta z = 250$  m, which is (barely) small enough to resolve the necessary vertical scales. In order to keep the aspect ratio of grid cells from becoming too large, the horizontal grid size is set to  $\Delta x = 500$  m. The time step of  $\Delta t = 0.5$  s is sufficient to satisfy the CFL criterion for these grid box dimensions.

Radiative cooling, expressed as an equivalent potential temperature source term, is set to  $-2$  K  $\text{d}^{-1}$  up to 12 km, tapering linearly to zero at 15 km. The radiative-convective equilibrium calculation is run with a mean wind in the  $y$  direction (normal to the plane of the two-dimensional calculation) of  $5$  m  $\text{s}^{-1}$  and an SST of 303 K. The  $y$  component of the mean wind, which is maintained by setting the relaxation constant  $\lambda_d = 5 \times 10^{-5}$   $\text{s}^{-1}$ , has no direct effect on the two-dimensional dynamics of the convection and is employed only to increase surface heat fluxes from their no-wind values.

We average the last 35 d of a 58 d calculation to obtain the sounding shown in figure 1. The system is approximately steady in a statistical sense during this interval, and the mean rainfall rate is approximately  $4.5$  mm  $\text{d}^{-1}$ . Notice that the relative humidity,  $\approx (s - s_d)/(s_s - s_d)$ , is quite high near the surface in the sounding, but decreases to near-zero above

about 300 hPa.

The sounding shown in figure 1 serves as the reference sounding for the WTG calculations presented in the next section. In these calculations we set  $\lambda_t = 1.5 \times 10^{-4} \text{ s}^{-1}$  and vary the  $y$  component of the wind and the SST in order to impose different values of the surface heat flux. The specified value of  $\lambda_t^{-1}$  is  $\approx 2 \text{ h}$ , or about the time required for a  $50 \text{ m s}^{-1}$  gravity wave to cross a 300 km convective domain.

The fact that  $\lambda_t^{-1}$  is not small compared to the lifetime of a convective cell means that the WTG assumption is not strictly observed. In particular, regimes with strong convection tend to develop slightly more stable soundings with cooler surface conditions and warmer conditions aloft than those with weak convection. However, the results are only weakly sensitive to the variations of  $\lambda_t$  in the  $(0.5 \text{ h})^{-1}$  to  $(2 \text{ h})^{-1}$  range, with only small variations in the equilibrium rainfall rate and in the time required to reach equilibrium for this range of values. For  $\lambda_t = (6 \text{ h})^{-1}$ , the equilibrium rainfall rate decreases by about 30% (for an imposed wind speed of  $10 \text{ m s}^{-1}$ ) as a result of the warming of the environment and the resulting lower relative humidity. Thus, the value  $\lambda_t = 1.5 \times 10^{-4} \text{ s}^{-1} \approx (2 \text{ h})^{-1}$  used in our calculations is close to the minimum needed to produce precipitation rates consistent with a strict application of the WTG approximation.

Figure 2 shows a high time resolution (5 min) time segment of various domain-averaged parameters for the radiative-convective equilibrium calculation. The 50 km domain is too small to support continuous deep convection, given the weakness of the radiative cooling, so convective bursts occur every 10 – 20 h. The surface evaporation recharges the convective environment between bursts, and convection is triggered when a measure of convective inhibition called DCIN decreases to a critical level.

DCIN, or deep convective inhibition index, was introduced by R2003 to characterize the convective inhibition of a deep, potentially unstable layer, and is defined for our purposes here as

$$\text{DCIN} = s_s(1750 - 2000) - s(0 - 1000) \equiv s_t - s_b \quad (24)$$

where the first term  $s_t$  is the threshold entropy for convection, defined as the saturated moist entropy averaged over the height range 1750 – 2000 m, and the second term  $s_b$  is the boundary layer entropy, defined as the moist entropy averaged over 0–1000 m. DCIN differs from a more conventional convective inhibition index in that a thicker layer of air is assumed to participate in the formation of a deep convective thermal.

Deep convection is triggered when DCIN decreases to a threshold value of about  $-20 \text{ J kg}^{-1} \text{ K}^{-1}$ . Downdrafts produced by the convection immediately increase DCIN to a stable value, from which it gradually recovers to initiate the next round of convection. The precipitable water also oscillates, with a gradual increase between convective pulses and a more rapid decrease during convection.

As figure 3 shows, fluctuations in DCIN result from fluctuations in both the boundary layer entropy and the threshold entropy. Fluctuations in these two quantities contribute with about equal magnitude. Dry-adiabatic subsidence in the presence of deep convection warms the layer just above the planetary boundary layer, thereby increasing  $s_t$ . At the same time, convective downdrafts reach the surface, decreasing  $s_b$ . Recovery from these perturbations occurs at about the same rate for both variables.

Figure 4 shows the evolution of the convective cell which initiated the rainfall episode near 54 h in figure 2. Updrafts of  $10 \text{ m s}^{-1}$  or greater occur at middle to upper levels. Evaporation of precipitation initiates downdrafts almost this strong in the decay phase of the cell. The development and spread of the cold pool at the surface is evident in the dry entropy field.

## 5 Results

WTG calculations were done for imposed  $y$  component winds of 0, 3, 5, 6, 7, 8, 9, 10, 15, and  $20 \text{ m s}^{-1}$  and for an SST of 303 K. Calculations were started with the radiative-convective equilibrium sounding described in the previous section and allowed to evolve for

23 d. Convection was initiated with a single warm bubble, but rapid randomization of the flow was assured by the additional imposition of random perturbations in the mixing ratio at the initial time. The time series of rainfall rate and precipitable water are shown in figures 5 - 8 for various imposed wind speeds.

If the reference state were truly an equilibrium state under the WTG approximation, then figure 5 should show steady precipitable water and a precipitation rate equal on the average to the radiative-convective equilibrium value of  $4.5 \text{ mm d}^{-1}$ , since the imposed wind and SST are the same as for the reference calculation. Instead, there is a slow decreasing trend in both precipitation rate and precipitable water, indicating that the reference state differs slightly from the equilibrium state. This may indicate that the initial radiative-convective equilibrium calculation was not run quite long enough to reach a true equilibrium state. However, a more likely explanation for this discrepancy is discussed later.

Figures 6, 7, and 8 show the evolution of the rainfall and precipitable water for imposed wind speeds of 0, 10, and  $20 \text{ m s}^{-1}$ . In each case the flow evolves toward a new equilibrium state with equilibrium rainfall rate and precipitable water both being increasing functions of imposed wind speed. The time required to reach the new equilibrium decreases with increasing wind speed.

Figure 9 shows the mean vertical mass flux, equal to the density times the WTG vertical velocity, averaged over the last quarter of the simulations when an equilibrium state has generally been reached. Results are shown for imposed wind speeds equal to 0, 5, 10, and  $20 \text{ m s}^{-1}$ . The two strongest wind cases have mass fluxes increasing upward almost to the tropopause. In the zero wind case, no convection occurs in the averaging period, and the downward mass flux is totally due to the imposed radiative cooling. In the  $5 \text{ m s}^{-1}$  case shallow convection predominates, with downward mass flux near 750 hPa due to the evaporation of cloud water by the surrounding dry air.

The mass flux profile predicted by the model is more top-heavy than is commonly seen in observations, e. g., Mapes and Houze (1993, 1995). Preliminary tests suggest that this

top-heavy profile is *not* due to any of the following factors: (1) effect of the top-heavy shape of the radiative cooling profile on the radiative-convective equilibrium reference state; (2) suppression of mesoscale dynamics by the small size of the computational domain; (3) two-dimensionality of the computation. However, comparison of the reference radiative-convective equilibrium sounding with observed soundings in the eastern and western tropical Pacific indicates that the static stability (defined as the vertical derivative of potential temperature) in this reference profile is too low by about a factor of two between 10 km and the tropopause, averaging  $1 \text{ K km}^{-1}$  compared to observed values of about  $2 \text{ K km}^{-1}$ . The weaker than observed static stability at upper levels could be responsible for the excessive upward mass fluxes there. This possibility will be explored in future work.

Figure 10 shows the domain- and time-averaged soundings for the last 6 d of the simulations corresponding to the mass fluxes in figure 9. As expected, the higher wind cases with higher rainfall rates exhibit higher moist entropy values, and hence higher humidities. The case with an imposed wind of  $5 \text{ m s}^{-1}$  has a weak stable layer near 700 hPa. Since this stable layer is not imposed from the outside, it must be a reflection of the existence of shallow convection which tops out near the level of the inversion, an interpretation supported by the corresponding mass flux profile in figure 9. This layer is possibly a consequence of the evaporation of cloud water near the tops of the small clouds. However, this merits further study.

The difference between the soundings in panels C and D of figure 10 is very small – the case with  $20 \text{ m s}^{-1}$  wind is slightly more stable than the  $10 \text{ m s}^{-1}$  case, but the relative humidity for the two cases is nearly identical.

Two calculations were performed with imposed wind of  $5 \text{ m s}^{-1}$  but with SSTs higher or lower than 303 K by 2 K. The case with SST equal to 301 K evolves into a low humidity state with no rain, which is quite similar to the case with SST equal 303 K and zero imposed wind. On the other hand, the 305 K case produces a sounding and rainfall rate quite similar to those found in the case with SST equal to 303 K and imposed wind of  $9 \text{ m s}^{-1}$ . This

similarity is not surprising in that increasing the wind speed and increasing the SST both act on convection solely via their effect on the surface moist entropy flux.

Calculations were made in which different starting humidity profiles are used with the same reference soundings, imposed winds, and SSTs. The precipitable water and rainfall rate converged to the same values in these calculations, indicating that the equilibrium states found are likely to be unique functions of the above three quantities. This is in contrast to the results of Raymond and Zeng (2000), in which two equilibrium states were generally found, even with cloud-radiation interactions turned off.

Figure 11 shows how the equilibrium rainfall rate and the surface entropy flux vary with imposed wind speed. When the surface entropy flux exceeds the radiative loss rate of entropy, the rainfall begins to increase from near-zero. This is consistent with R2000. It is important to remember that these plots represent *equilibrium* conditions, and that non-equilibrium states deviate from these results. For instance, as figure 8 shows, the initial imposition of strong surface fluxes on a dry atmosphere doesn't instantly result in intense rainfall.

A curious feature of figure 11 is that the WTG simulation with imposed wind of  $5 \text{ m s}^{-1}$  does not reproduce the results of the radiative-convective equilibrium reference calculation with the same imposed wind speed. In particular, the precipitation rate is much less than the radiative-convective equilibrium value of  $\approx 4.5 \text{ mm d}^{-1}$ , in spite of the fact that the surface and radiative entropy fluxes nearly balance. This discrepancy is also evident in figure 5. We believe that this occurs because the WTG calculation, by virtue of the relaxation constraints imposed on the potential temperature and mixing ratio profiles, does not reproduce the full *ensemble* of states occurring in the radiative-convective equilibrium calculation. Close comparison of the two simulations shows in particular that the mean surface moisture flux is slightly less in the WTG calculation than in radiative-convective equilibrium. This appears to result from the tendency of the lateral entrainment to relax the surface humidity back to the reference value more rapidly than would be produced by surface fluxes by themselves, thus weakening these fluxes. However, the results are sufficiently complex that other similar

factors could be coming into play as well.

Figure 12 shows values of rainfall rate plotted versus saturation fraction (precipitable water divided by the precipitable water of a fully saturated environment with the same temperature profile) sampled after smoothing by a low pass filter with a 12 h cutoff. As hypothesized by R2000, to a good approximation, the (smoothed) rainfall rate is a unique function of the saturation fraction. This is true even in the *transient* case, as figure 12 shows.

## 6 Conclusions

The results of our cumulus ensemble calculations tend to support the conclusions reached by R2000. In particular, we find that

1. rainfall is related in the steady state to the imbalance between the gain in column moist entropy (or moist static energy) due to surface heat fluxes, and its loss due to radiation;
2. rainfall is a nearly unique function of precipitable water (or saturation fraction), even when the atmosphere is still adjusting to altered forcing;
3. the adjustment time to reach a steady state is inversely related to the strength of the entropy imbalance.

Different behaviors are seen for moist and dry soundings. For relatively dry soundings, the rainfall rate is determined by the saturation fraction, as indicated by figure 12. The imbalance between surface entropy fluxes and radiative losses determines the *tendency* of precipitation rate, with a positive imbalance leading to increasing saturation fraction with time and increasing rainfall rates. For more moist atmospheres, the rainfall rate becomes a very sensitive function of the sounding, with the saturation fraction eventually asymptoting to a limiting value. Under these conditions the atmosphere adjusts very rapidly to changes in surface fluxes, which means that in practice the surface moist entropy flux is a

better predictor of rainfall rate than the saturation fraction of the sounding for very moist atmospheres.

Interestingly, multiple equilibrium states, as found by Raymond and Zeng (2000) in a two-column model employing a cumulus parameterization, do not appear to exist in this case. If this result holds up, it simplifies tropical dynamics by providing the assurance that large-scale forcing causes evolution of the atmospheric column toward a unique state. However, cloud-radiation interactions, which caused the most robust tendency toward multiple equilibria in Raymond and Zeng (2000), are not invoked in the current work.

The fact that the surface entropy flux is a good predictor of rainfall when the environment is already moist may explain why the correlation between surface moist entropy flux and rainfall rate is strong in the normally moist atmospheres of the east and west Pacific warm pools (Raymond, 1995; R2003). This correlation is observed to be weaker in areas such as Kwajalein, which is on the boundary of equatorial moist air, and is therefore subject to large moisture variations due to advection (Sobel et al., 2003).

This brings to light one simplification shared by both R2000 and the present work: Differential moisture advection by a sheared mean flow is ignored. In regions with strong shears and significant horizontal moisture gradients, such advection may be important in controlling the column precipitable water, and hence the saturation fraction and precipitation rate. However, this effect is straightforward to incorporate into the moisture budgets of large-scale models, and is ignored here for the sake of clarity.

The differences between R2000 and the present results are primarily in quantitative detail. One such difference is that the rainfall rate in the present study asymptotes to large values for a saturation fraction less than unity, whereas this asymptote is assumed to occur for 100% saturation in the column in R2000. Furthermore, the rainfall rate goes to zero for finite values of the saturation fraction, whereas small, but non-zero precipitation rates are assumed for all saturation fractions in R2000. However, these differences are remarkably minor given the vast difference in the complexity of the two models.

The present results have the limitation that only a small, two-dimensional domain is used to simulate the convection. This eliminates the development of mesoscale convective systems and makes the simulation of individual convective cells somewhat unrealistic. These restrictions will be lifted in future work.

*Acknowledgments.* We thank Adam Sobel and an anonymous reviewer for many useful comments. This work was supported by US National Science Foundation grant ATM-0079984.

## 7 Appendix

More details are given on the cloud model in this appendix.

The conversion between total advected water and precipitation is governed by the term  $S_{cr}$ , which is assumed to equal

$$S_{cr} = \begin{cases} -\lambda_r(r_t - r_s), & r_t > r_s \\ -\lambda_e r_r(r_t - r_s), & r_t < r_s \end{cases} \quad (25)$$

where  $r_s$  is the saturation mixing ratio and  $\lambda_r$  and  $\lambda_e$  are specified constants. We find  $\lambda_r = 0.01 \text{ s}^{-1}$  and  $\lambda_e = 1 \text{ s}^{-1}$  to be satisfactory values. This scheme is very simple, but it has the advantage that the high relative humidities produced aloft by warm rain schemes such as the Kessler parameterization do not occur.

For reasons of computational speed, a simplified version of the equivalent potential temperature is used:

$$\theta_e = \theta \exp(\alpha r) \quad (26)$$

where  $\alpha = (L_c + L_f)/(C_p T_R)$ . The quantities  $L_c$  and  $L_f$  are the latent heats of condensation and freezing,  $r$  is the water vapor mixing ratio,  $\theta$  is the potential temperature, and  $C_p$  is the specific heat of air at constant pressure. The saturation mixing ratio is given by  $r_s = \epsilon e_s(T)/p$ , where  $\epsilon$  is the ratio of the molecular weights of vapor and air and where the

saturation vapor pressure of water (in pascals) is approximated by Tetens' formula,

$$e_s(T) = 611.2 \exp[17.67(T - 273.15)/(T - 29.65)], \quad (27)$$

$T$  being the temperature in kelvins.

The eddy mixing coefficient is given by

$$K = \rho C \left[ \sum_{i,j} D_{ij} D_{ij} - \frac{2g}{\theta} \Gamma_e \right]^{1/2} \Delta z^2 \quad (28)$$

where  $g$  is the acceleration of gravity. We set  $K = 0$  when the quantity inside the square brackets is negative. In the case of pure vertical shear of the horizontal wind, this occurs when the Richardson number exceeds 0.25. The vertical grid size is  $\Delta z$ ,  $C = 1$ , and  $\Gamma_e$  is the effective static stability. This switches between a dry and a moist value depending on a generalized relative humidity  $H = r_t/r_s$ :

$$\Gamma_e = A \frac{\partial \theta_e}{\partial z} + (1 - A) \frac{\partial \theta}{\partial z}, \quad (29)$$

with a switching function  $A = [(H - 1)/\delta H + 1]/2$ , where  $\delta H = 0.02$  and where  $A$  is limited to the range  $0 \leq A \leq 1$ . The gradual switch emulates situations in which a grid box is partially saturated and partially unsaturated, and also avoids numerical problems which can occur with the eddy mixing turning on and off instantaneously.

The surface flux sources are concentrated in the lowest model layer and are derived from a bulk flux formula. For example, the entropy surface source term is

$$S_{es} = C_d U_e [\theta_{ess} - \theta_e(0)] / (\Delta z / 2) \quad (30)$$

where  $C_d = 0.001$  is the drag coefficient,  $\theta_{ess}$  is the saturated sea surface equivalent potential temperature,  $\theta_e(0)$  is the equivalent potential temperature of the air at the lowest model

level, and where the effective surface wind speed is

$$U_e = [v_x(0)^2 + v_y(0)^2 + W^2]^{1/2}. \quad (31)$$

The quantities  $v_x(0)$  and  $v_y(0)$  are the surface wind components and  $W = 3 \text{ m s}^{-1}$  accounts for the effects of local gustiness. Similar equations obtain for the mixing ratio and the wind stress. The same drag coefficient is used for the stress and the thermodynamic fluxes.

The flux-conservative Lax-Wendroff numerical scheme is used for all fields. The contributions of eddy mixing, the external sink terms, and the precipitation generation are only included in the final step of the Lax-Wendroff scheme, since a very short time step is dictated by the CFL criterion on sound waves, resulting in little error in the evaluation of the terms representing the above slower processes.

The horizontal eddy mixing coefficient is defined

$$K_h = \lambda_f \Delta^2 / 4 \quad (32)$$

where  $\Delta \equiv \Delta x = \Delta y$  is the horizontal grid size and  $\lambda_f$  is a specified rate constant. This term is needed to damp  $2\Delta x$  oscillations which otherwise develop as the result of the nonlinear cascade of energy to small scales. A value of  $\lambda_f = 0.003 \text{ s}^{-1}$  is sufficient to accomplish this.

## 8 References

- Grabowski**, W. W., and M. W. Moncrieff, 2001: Large-scale organization of tropical convection in two-dimensional explicit numerical simulations. *Quart. J. Roy. Meteor. Soc.*, **127**, 445-468.
- Grabowski**, W. W., X. Wu, M. W. Moncrieff, and W. D. Hall, 1998: Cloud-resolving modeling of cloud systems during phase III of GATE. Part II: Effects of resolution and the third spatial dimension. *J. Atmos. Sci.*, **55**, 3264-3282.

- Grabowski, W. W., X. Wu, and M. W. Moncrieff, 1996:** Cloud-resolving modeling of tropical cloud systems during phase III of GATE. Part I: Two-dimensional experiments. *J. Atmos. Sci.*, **53**, 3684-3709.
- Grabowski, W. W., X. Wu, and M. W. Moncrieff, 1999:** Cloud resolving modeling of tropical cloud systems during phase III of GATE. Part III: Effects of cloud microphysics. *J. Atmos. Sci.*, **56**, 2384-2402.
- Mapes, B., and R. A. Houze, Jr., 1993:** An integrated view of the 1987 Australian monsoon and its mesoscale convective systems. II: Vertical structure. *Quart. J. Roy. Meteor. Soc.*, **119**, 733-754.
- Mapes, B., and R. A. Houze, Jr., 1995:** Diabatic divergence profiles in western Pacific mesoscale convective systems. *J. Atmos. Sci.*, **52**, 1807-1828.
- Neelin, J. D., and I. M. Held, 1987:** Modeling tropical convergence based on the moist static energy budget. *Mon. Wea. Rev.*, **115**, 3-12.
- Nilsson, J., and K. A. Emanuel, 1999:** Equilibrium atmospheres of a two-column radiative-convective model. *Quart. J. Roy. Meteor. Soc.*, **125**, 2239-2264.
- Randall, D. A., K.-M. Xu, R. J. C. Somerville, and S. Iacobellis, 1996:** Single-column models and cloud ensemble models as links between observations and climate models. *J. Climate*, **9**, 1683-1697.
- Raymond, D. J., 1995:** Regulation of moist convection over the west Pacific warm pool. *J. Atmos. Sci.*, **52**, 3945-3959.
- Raymond, D. J., 2000:** Thermodynamic control of tropical rainfall. *Quart. J. Roy. Meteor. Soc.*, **126**, 889-898.
- Raymond, D. J., G. B. Raga, C. S. Bretherton, J. Molinari, C. López-Carrillo, Ž. Fuchs, 2003:** Convective forcing in the intertropical convergence zone of the east Pacific. *J.*

*Atmos. Sci.*, **60**, 2064-2082.

**Raymond**, D. J., and X. Zeng, 2000: Instability and large-scale circulations in a two-column model of the tropical troposphere. *Quart. J. Roy. Meteor. Soc.*, **126**, 3117-3135.

**Robe**, F. R., and K. Emanuel, 1996: Moist convective scaling: Some inferences from three-dimensional cloud ensemble simulations. *J. Atmos. Sci.*, **53**, 3265-3275.

**Robe**, F. R., and K. A. Emanuel, 2001: The effect of vertical wind shear on radiative-convective equilibrium states. *J. Atmos. Sci.*, **58**, 1427-1445.

**Sobel**, A. H., and C. S. Bretherton, 2000: Modeling tropical precipitation in a single column. *J. Climate*, **13**, 4378-4392.

**Sobel**, A. H., S. E. Yuter, C. S. Bretherton, and G. N. Kiladis, 2003: Large-scale meteorology and deep convection during TRMM KWAJEX. *Mon. Wea. Rev.*, in press.

**Sui**, C. H., K. M. Lau, W. K. Tao, and J. Simpson, 1994: The tropical water and energy cycles in a cumulus ensemble model. Part I: Equilibrium climate. *J. Atmos. Sci.*, **51**, 711-728.

**Tompkins**, A. M., 2001a: On the relationship between tropical convection and sea surface temperature. *J. Climate*, **14**, 633-637.

**Tompkins**, A. M., 2001b: Organization of tropical convection in low vertical wind shears: The role of water vapor. *J. Atmos. Sci.*, **58**, 529-545.

**Tompkins**, A. M., and G. C. Craig, 1998a: Radiative-convective equilibrium in a three-dimensional cloud-ensemble model. *Quart. J. Roy. Meteor. Soc.*, **124**, 2073-2097.

**Tompkins**, A. M., and G. C. Craig, 1998b: Time-scales of adjustment to radiative-convective equilibrium in the tropical atmosphere. *Quart. J. Roy. Meteor. Soc.*, **124**, 2693-2713.

**Tompkins**, A. M., and G. C. Craig, 1999: Sensitivity of tropical convection to sea surface temperature in the absence of large-scale flow. *J. Climate*, **12**, 462-476.

**Xu**, K.-M., and D. A. Randall, 1999: A sensitivity study of radiative-convective equilibrium in the tropics with a convection-resolving model. *J. Atmos. Sci.*, **56**, 3385-3399.

## 9 Figures

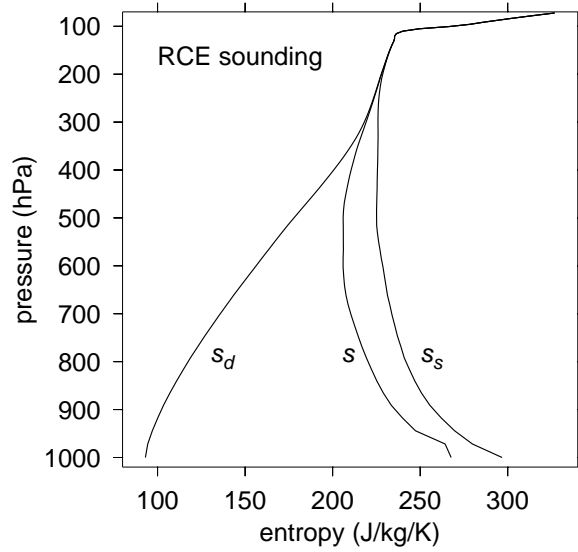


Figure 1: Dry entropy ( $s_d$ ), moist entropy ( $s$ ), and saturated moist entropy ( $s_s$ ) as a function of pressure for radiative-convective equilibrium sounding.

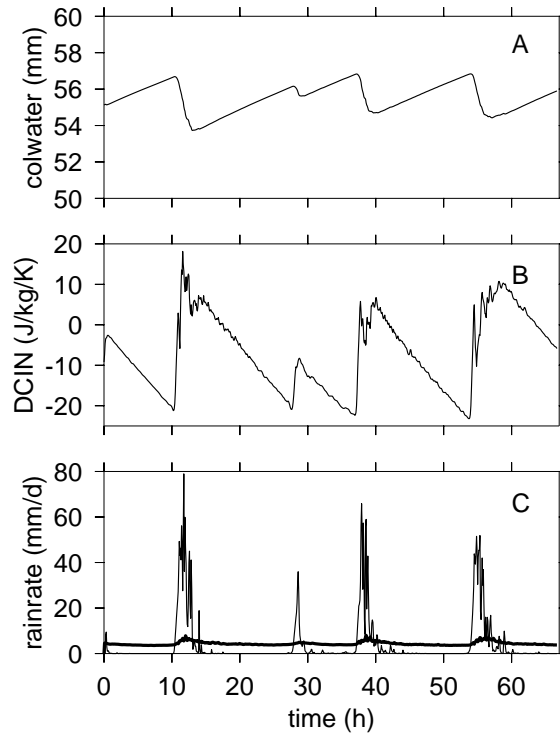


Figure 2: High resolution time segment of radiative-convective equilibrium calculation, averaged over the domain. (a) Column-integrated precipitable water. (b) Deep convective inhibition index DCIN. (c) Rainfall rate (thin line) and evaporation rate (thick line).

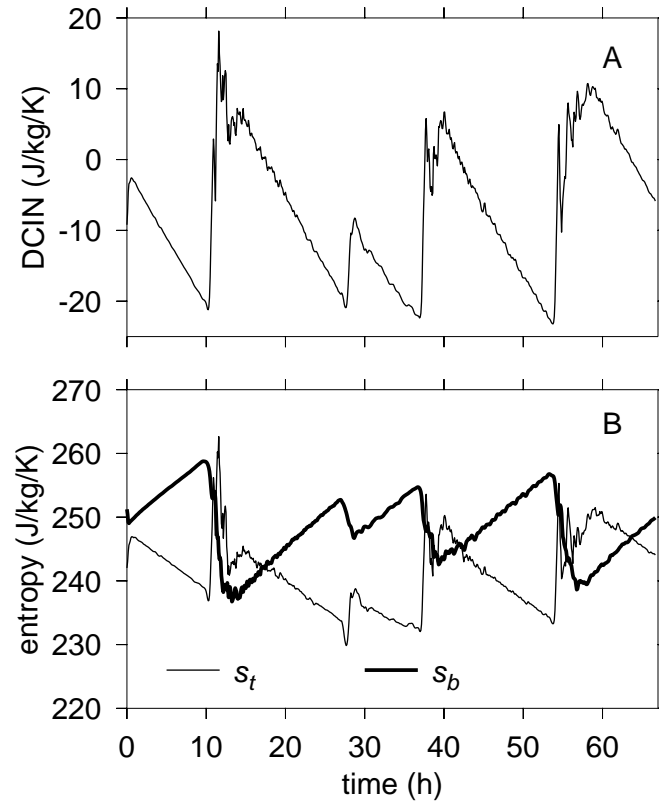


Figure 3: Components contributing to DCIN. (a) Plot of domain-averaged DCIN as a function of time. (b) Domain averaged threshold entropy ( $s_t$ ) and boundary layer entropy ( $s_b$ ).

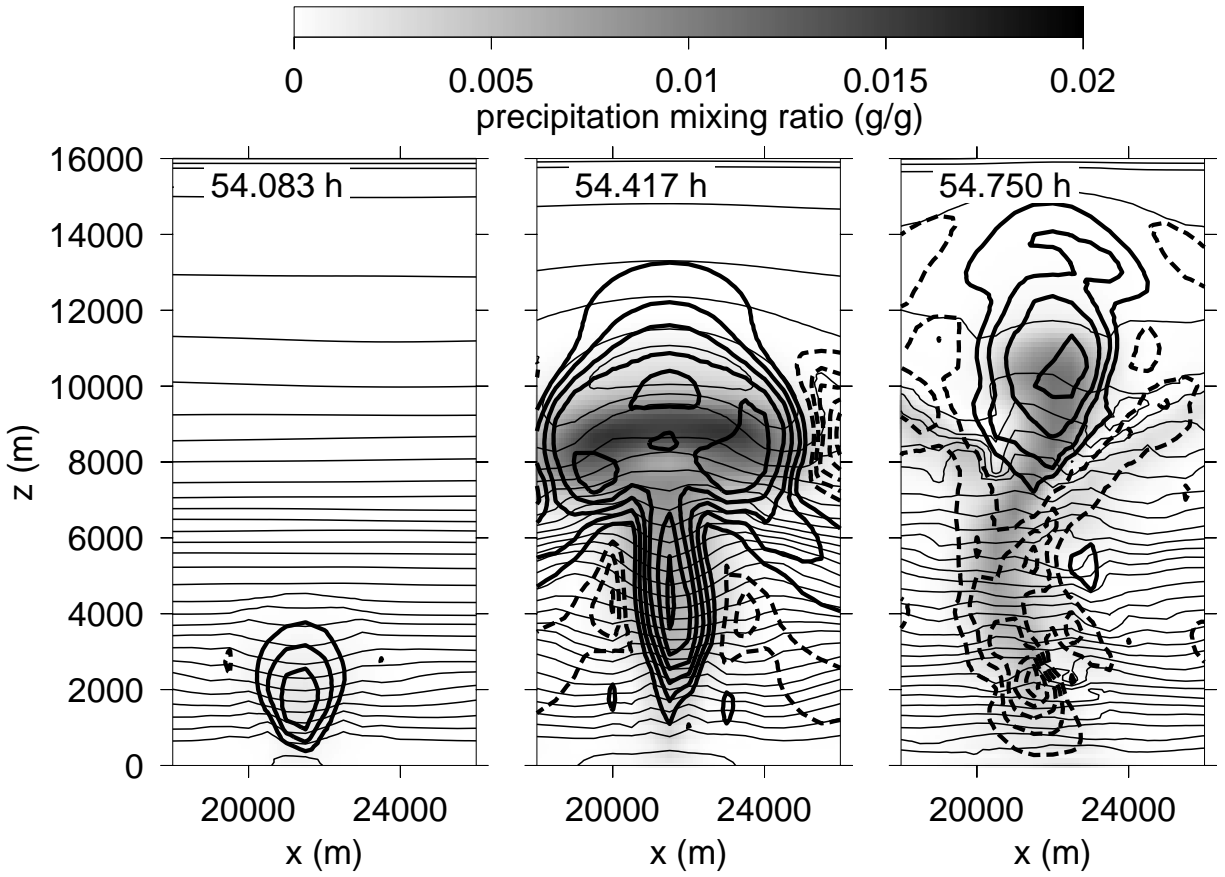


Figure 4: Three snapshots of convective cell occurring near 54 h in figure 2. The heavy contours are vertical wind with contour interval  $2 \text{ m s}^{-1}$ . Negative contours are dashed and the zero contour is suppressed. The thin contours represent dry entropy at intervals of  $5 \text{ J kg}^{-1} \text{ K}^{-1}$ . The shading represents precipitation mixing ratio.

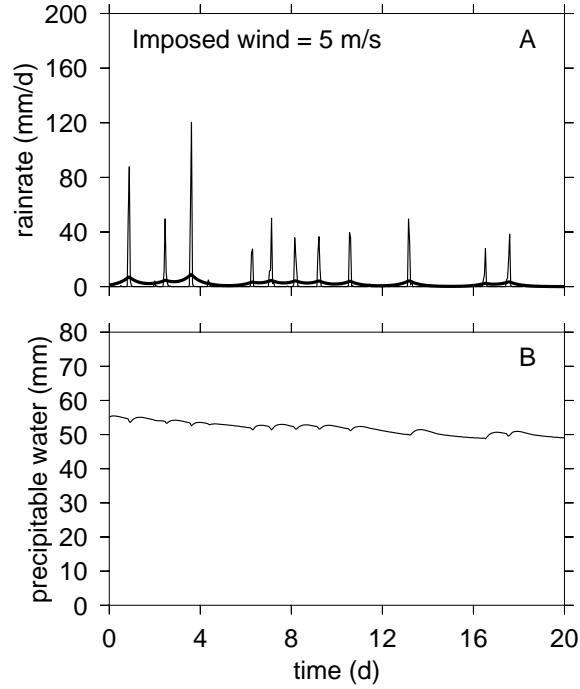


Figure 5: Time series for the WTG simulation with imposed wind of  $5 \text{ m s}^{-1}$  and SST of 303 K. (a) Domain-averaged rainfall rate as a function of time. The heavy line is the low pass filtered rainfall rate with a cutoff period of 12 h. (b) Domain-averaged precipitable water as a function of time.

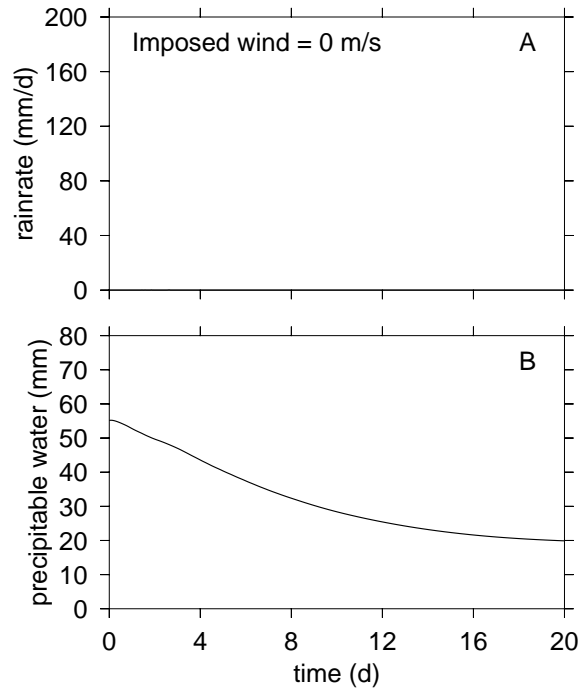


Figure 6: As in figure 5 except imposed wind of  $0 \text{ m s}^{-1}$ .

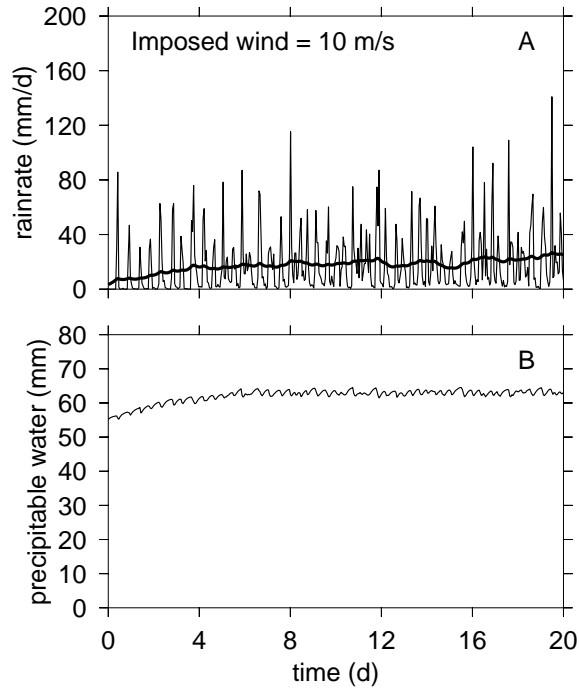


Figure 7: As in figure 5 except imposed wind of  $10 \text{ m s}^{-1}$ .

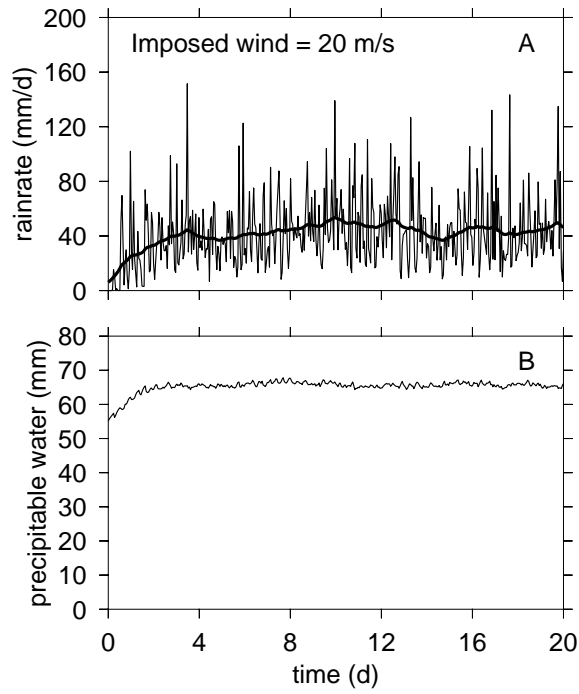


Figure 8: As in figure 5 except imposed wind of  $20 \text{ m s}^{-1}$ .

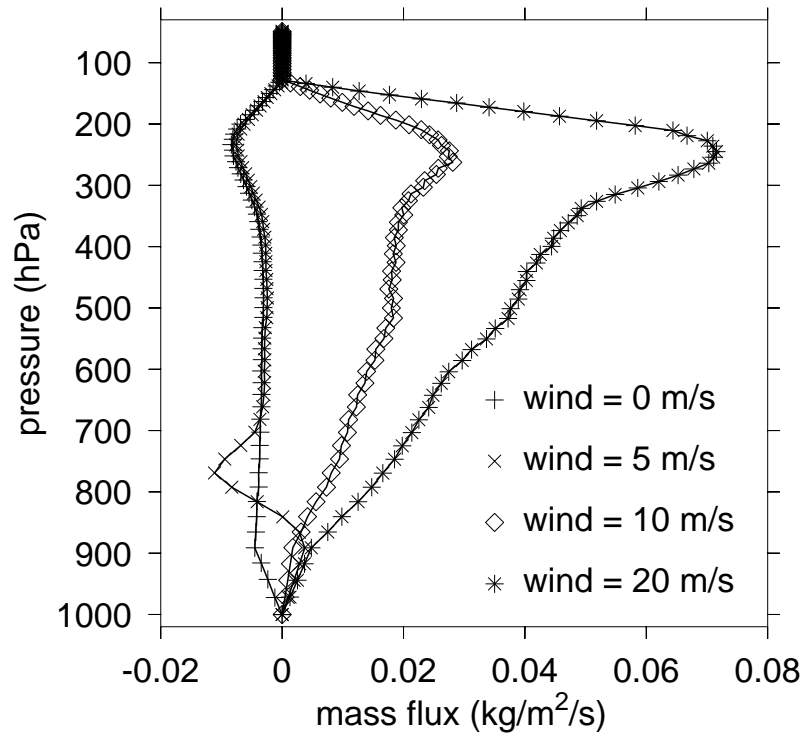


Figure 9: Mean vertical mass flux averaged over last 6 d of each simulation for the imposed wind speeds listed. In each case the mass flux is the WTG vertical velocity times the density.

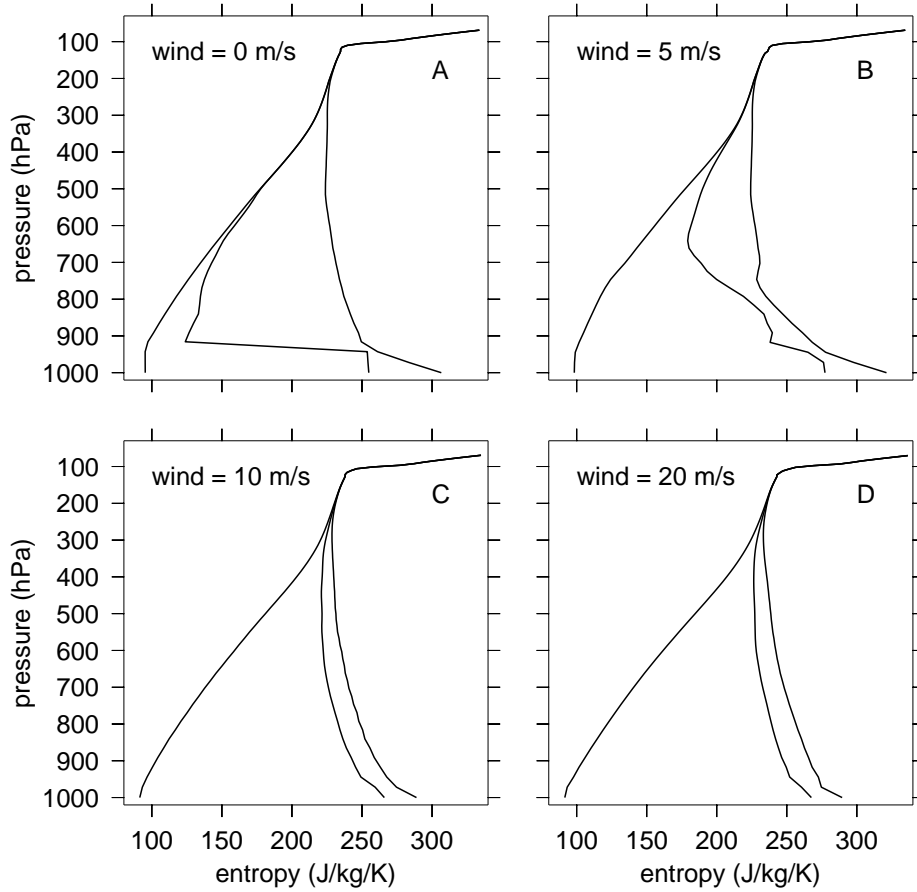


Figure 10: Mean soundings for the last 6 d of the simulations corresponding to the mass flux profiles shown in figure 9. See figure 1 for meaning of plots.

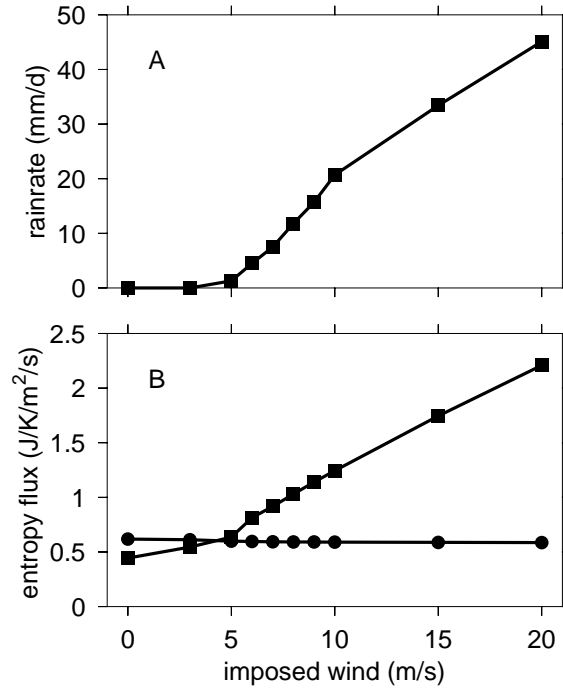


Figure 11: Equilibrium plots of (a) rainfall rate versus imposed wind speed and (b) surface entropy flux (filled boxes) and radiative entropy sink (bullets) as a function of wind speed.

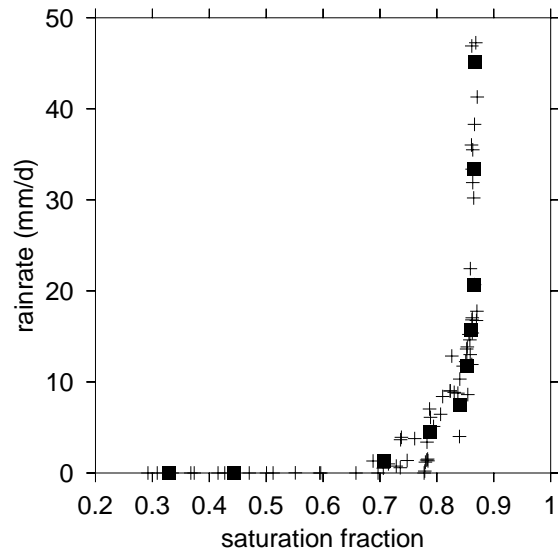


Figure 12: Plot of smoothed rain rate versus smoothed saturation fraction. The filled boxes show the respective values in the WTG equilibrium state for various imposed wind speeds and the pluses show transient values occurring during the relaxation toward equilibrium in the WTG calculations.